Supplementary Materials for

The Wiedemann-Franz law in doped Mott insulators without quasiparticles

Wen O. Wang *et al*.

Corresponding authors: Wen O. Wang, wenwang.physics@gmail.com; Thomas P. Devereaux, tpd@stanford.edu

Science **382**, 1070 (2023)
DOI: 10.1126/science.ade3232

The PDF file includes:

Methods

Simulation Parameters

Simulations of the 2D single-band t-t'-U Hubbard model in the grand canonical ensemble were performed on 8×8 square lattice clusters (unless otherwise specified), with periodic boundary conditions, next-nearest-neighbour hopping $t' = -0.25t$ or 0, and on-site Coulomb repulsion U between $6t$ and $10t$. For convenience, k_B, $\hbar$, and charge e are set to 1 throughout the paper. Measurements of all quantities, other than particle density $\langle n \rangle$ in the chemical potential tuning process described later, if not otherwise specified, were performed with an imaginary time Trotter discretization $d\tau = 0.05/t$ (*30, 31*). At high temperatures, the smallest number of imaginary time slices used in the Trotter decomposition was $\tilde{L} = \beta/d\tau = 20$, where β is the inverse temperature T^{-1}. Each Markov chain in the Monte Carlo process consisted of 5×10^4 warm up sweeps and 10^6 measurement sweeps through space-time. Unequal time measurements were taken every 4 sweeps. Measurements were made on up to ~ 2400 Markov chains for each set of parameters at the lowest temperatures, with 2.5×10^5 unequal time measurements and approximately $2 \times 10^5 \times \tilde{L}$ equal time measurements per chain.

Analytic Continuation

We evaluated DC transport coefficients using the Kubo formula for κ and σ (*35*). The DC transport coefficients were obtained by performing maximum entropy analytic continuation (MaxEnt) (*32,33*) on DQMC measurements of corresponding correlation functions in imaginary time. To determine the adjustable parameter which assigns weights of statistics and entropy in the maximized function in MaxEnt, we use the method of Ref. (*43*). Details of the formalism, operators, and specific correlation functions can be found in the "Formalism" subsection of the Supplementary Text.

The MaxEnt algorithm requires a "model" function to regularize the real-frequency correlation function. In this work, we used an annealing procedure in which spectra from one temperature serve as the model function for the next lower temperature in a sequence (*26, 35*). We determined spectra in the infinite-temperature limit using the moments expansion method (*26, 35*) (up to sixth order for $t'/t = -0.25$, or eighth order for $t' = 0$), and used these spectra as the model functions at the highest temperature. Although the choice of model function may impact the result of the MaxEnt analysis, this variation does not significantly affect the quantitative results and the qualitative behavior and conclusions remain unchanged (see Fig. S8 in the Supplementary Text).

Chemical Potential Tuning

To tune the chemical potential μ for a specific target filling $n_{\text{tar}} = 1 - p_{\text{tar}}$ at a given temperature and lattice size, we used DQMC to calculate $\langle n \rangle$ over a range of chemical potentials μ (at $0.05t$ intervals). We obtained the best μ by interpolation of $\langle n \rangle$ versus μ. For the tuning process, the maximum imaginary time discretization $d\tau$ was chosen to be $0.02/t$, and at high temperatures, the smallest number of imaginary-time slices was $\tilde{L} = 20$. The doping p in each figure indicates the target doping p_{tar}.

Error Analysis

Error bars are shown for all measurements. If not otherwise specified, error bars are determined by bootstrap resampling (*44*). In particular, we calculated 100 bootstraps and used the standard deviation of the distribution as the standard error of the mean. The mean values represent the average values from bootstrap resampling. For analytic continuation, the average spectra from bootstrap resampling at one temperature served as the model function for the next lower temperature, as described above for annealing.

Supplementary Text

Formalism

In this paper, κ refers to the longitudinal DC thermal conductivity measured under the condition of zero charge current (*35*), distinguished from the one measured under the condition of zero electric field; c_v refers to the specific heat, defined as the energy density difference of the system per temperature difference at fixed density.

We investigate the 2D single-band Hubbard model with spin $S = 1/2$. Considering both nearest-neighbour t and the next-nearest-neighbour t' hopping, the Hamiltonian is

$$\begin{aligned}\hat{H} &= -t\sum_{\langle lm\rangle\sigma}\left(c^\dagger_{l\sigma}c_{m\sigma}+c^\dagger_{m\sigma}c_{l\sigma}\right)-t'\sum_{\langle\langle lm\rangle\rangle\sigma}\left(c^\dagger_{l\sigma}c_{m\sigma}+c^\dagger_{m\sigma}c_{l\sigma}\right)\\ &\quad +U\sum_{l}\left(n_{l\uparrow}-\tfrac{1}{2}\right)\left(n_{l\downarrow}-\tfrac{1}{2}\right),\end{aligned} \tag{S1}$$

where U is the on-site Coulomb interaction, $c^\dagger_{l,\sigma}$ $(c_{l,\sigma})$ is the creation (annihilation) operator for an electron at site l with spin σ, and $n_{l,\sigma} \equiv c^\dagger_{l,\sigma}c_{l,\sigma}$ is the number operator at site l with spin σ.

Expressions for κ, σ, and c_v have been derived in the Supplementary Material in Ref. (*35*). Calculating σ and κ requires correlation functions that include the particle/charge current $\mathbf{J}$ and energy current $\mathbf{J}_E$ terms. From the Hamiltonian in Eq. S1, we derive $\mathbf{J}$ and $\mathbf{J}_E$ in a manner similar to that in Ref. (*35*), obtaining

$$\begin{aligned}\mathbf{J} &= \tfrac{t}{2}\sum_{l,\boldsymbol{\delta}\in\mathrm{NN},\sigma}\boldsymbol{\delta}(ic^\dagger_{l+\delta,\sigma}c_{l,\sigma}+h.c.)\\ &\quad +\tfrac{t'}{2}\sum_{l,\boldsymbol{\delta}'\in\mathrm{NNN},\sigma}\boldsymbol{\delta}'(ic^\dagger_{l+\delta',\sigma}c_{l,\sigma}+h.c.)\end{aligned} \tag{S2}$$

and

$$
\begin{aligned}
\mathbf{J}_E \quad = & \sum_{l,\boldsymbol{\delta}_1\in\mathrm{NN},\boldsymbol{\delta}_2\in\mathrm{NN},\sigma} (-\tfrac{\boldsymbol{\delta}_1+\boldsymbol{\delta}_2}{4})t^2(ic^\dagger_{l+\delta_1+\delta_2,\sigma}c_{l,\sigma}+h.c.) \\
& + \sum_{l,\boldsymbol{\delta}\in\mathrm{NN},\boldsymbol{\delta}'\in\mathrm{NNN},\sigma} (-\tfrac{\boldsymbol{\delta}+\boldsymbol{\delta}'}{2})tt'(ic^\dagger_{l+\delta+\delta',\sigma}c_{l,\sigma}+h.c.) \\
& + \sum_{l,\boldsymbol{\delta}'_1\in\mathrm{NNN},\boldsymbol{\delta}'_2\in\mathrm{NNN},\sigma} (-\tfrac{\boldsymbol{\delta}'_1+\boldsymbol{\delta}'_2}{4})t'^2(ic^\dagger_{l+\delta'_1+\delta'_2,\sigma}c_{l,\sigma}+h.c.) \\
& + \tfrac{Ut}{4}\sum_{l,\boldsymbol{\delta}\in\mathrm{NN},\sigma} \boldsymbol{\delta}(n_{l+\delta,-\sigma}+n_{l,-\sigma})(ic^\dagger_{l+\delta,\sigma}c_{l,\sigma}+h.c.) \\
& + \tfrac{Ut'}{4}\sum_{l,\boldsymbol{\delta}'\in\mathrm{NNN},\sigma} \boldsymbol{\delta}'(n_{l+\delta',-\sigma}+n_{l,-\sigma})(ic^\dagger_{l+\delta',\sigma}c_{l,\sigma}+h.c.) \\
& - \tfrac{Ut}{4}\sum_{l,\boldsymbol{\delta}\in\mathrm{NN},\sigma} \boldsymbol{\delta}(ic^\dagger_{l+\delta,\sigma}c_{l,\sigma}+h.c.) \\
& - \tfrac{Ut'}{4}\sum_{l,\boldsymbol{\delta}'\in\mathrm{NNN},\sigma} \boldsymbol{\delta}'(ic^\dagger_{l+\delta',\sigma}c_{l,\sigma}+h.c.).
\end{aligned} \tag{S3}
$$

To make the notations above clear, NN (NNN) denotes the set of nearest-neighbour (next-nearest-neighbour) position displacements. Specifically, on the two-dimensional square lattice, $\mathrm{NN}=\{+\mathbf{x},-\mathbf{x},+\mathbf{y},-\mathbf{y}\}$ and $\mathrm{NNN}=\{+\mathbf{x}+\mathbf{y},-\mathbf{x}+\mathbf{y},+\mathbf{x}-\mathbf{y},-\mathbf{x}-\mathbf{y}\}$, where the lattice constant is set to 1 and $\mathbf{x}$ and $\mathbf{y}$ are unit vectors. Here, if l is an arbitrary site label associated with the position vector $\mathbf{R}_l = x_l\mathbf{x}+y_l\mathbf{y}$, and $\boldsymbol{\nu}$ is a vector adding up arbitrary elements in NN and NNN, the notation $l+\nu$ represents a unique site label associated with the position $x_l\mathbf{x}+y_l\mathbf{y}+\boldsymbol{\nu}$. The first three lines of Eq. S3 define the kinetic energy current $\mathbf{J}_K$, and the fourth to the seventh lines correspond to the potential energy current $\mathbf{J}_P$. The heat current is $\mathbf{J}_Q=\mathbf{J}_E-\mu\mathbf{J}$.

Fourier transforming the fermion operators

$$
c^\dagger_{l,\sigma} = \frac{1}{\sqrt{N}}\sum_{\mathbf{k}} e^{-i\mathbf{k}\cdot\mathbf{R}_l}c^\dagger_{\mathbf{k},\sigma}, \tag{S4}
$$

where N is the number of sites, we can transform Eq. S2, and the first three lines of Eq. S3 ($\mathbf{J}_K$), which yield

$$
\mathbf{J} = \sum_{\mathbf{k},\sigma}\mathbf{v}_{\mathbf{k}}c^\dagger_{\mathbf{k},\sigma}c_{\mathbf{k},\sigma}, \tag{S5}
$$

$$
\mathbf{J}_K = \sum_{\mathbf{k},\sigma}\epsilon_{\mathbf{k}}\mathbf{v}_{\mathbf{k}}c^\dagger_{\mathbf{k},\sigma}c_{\mathbf{k},\sigma}, \tag{S6}
$$

as summations in $\mathbf{k}$-space. Here, $\epsilon_{\mathbf{k}}$ is the band energy at momentum $\mathbf{k}$, determined by the $U=0$ non-interacting limit of the Hamiltonian in Eq. S1, $\hat{H}(U=0)=\sum_{\mathbf{k},\sigma}\epsilon_{\mathbf{k}}c^\dagger_{\mathbf{k},\sigma}c_{\mathbf{k},\sigma}$, and $\mathbf{v}_{\mathbf{k}}\equiv\partial\epsilon_{\mathbf{k}}/\partial\mathbf{k}$ is the band velocity.

The two-particle (four-fermion) contribution to $\mathbf{J}_P$ selects charge flow involving a process where an electron flows from/to a site already occupied by an electron of opposite spin. In other words, nonzero contributions to the two-particle contribution to $\mathbf{J}_P$ rely on breaking and reforming double occupancies, leading to L_P decreasing with increasing doping as double occupancies are reduced.

Using the Kubo formula, the transport coefficients are defined as (*35*)

$$L_{O_1O_2}(\omega) = \frac{1}{N\beta}\int_0^\infty dt e^{i(\omega+i0^+)t}\int_0^\beta d\tau \langle O_1(t-i\tau)O_2(0)\rangle, \tag{S7}$$

where O_1 and O_2 are Hermitian operators that can be chosen as any one of the current operators introduced previously, and $\beta = 1/T$ is the inverse temperature. Here, t is real-time, without confusion with the hopping matrix elements in the Hamiltonian, and

$$O_1(t-i\tau) = e^{i(\hat{H}-\mu\hat{N})(t-i\tau)}O_1 e^{-i(\hat{H}-\mu\hat{N})(t-i\tau)}, \tag{S8}$$

where $\hat{N}$ is the operator for the total number of particles in the system. For Hamiltonians such as Eq. S1, one can show $L_{O_1O_2}(\omega) = L_{O_2O_1}(\omega)$ from Eq. S7 for any operators O_1, $O_2 \in \{J_x$, $J_{Q,x}$, $J_{K,x}$, $J_{P,x}\}$ (*45*). We consider $O_1 = O_2 = O$, and set $Z = \mathrm{Tr}(e^{-\beta(\hat{H}-\mu\hat{N})})$ as the partition function. From Eq. S7, we obtain

$$\mathrm{Re}\, L_{OO}(\omega) = \frac{\pi}{ZN\beta\omega}\sum_{i_1,i_2}|\langle i_1|O|i_2\rangle|^2 e^{-\beta E_{i_1}}\left(1-e^{-\beta\omega}\right)\delta(\omega+E_{i_1}-E_{i_2}), \tag{S9}$$

where $|i_1\rangle$ (E_{i_1}) are eigenstates (eigenvalues) of $\hat{H}-\mu\hat{N}$. We use DQMC to measure the correlation functions in imaginary time

$$\begin{aligned}\langle T_\tau O(\tau)O(0)\rangle &\equiv \frac{1}{Z}\mathrm{Tr}\left(e^{-\beta(\hat{H}-\mu\hat{N})}T_\tau e^{\tau(\hat{H}-\mu\hat{N})}Oe^{-\tau(\hat{H}-\mu\hat{N})}O\right)\\ &= \frac{1}{Z}\sum_{i_1,i_2}|\langle i_1|O|i_2\rangle|^2 e^{-\beta E_{i_1}}e^{\tau(E_{i_1}-E_{i_2})}.\end{aligned} \tag{S10}$$

We then apply MaxEnt (*32, 33*) to $\langle T_\tau O(\tau)O(0)\rangle$ and obtain $\mathrm{Re}\, L_{OO}(\omega)$ (*26, 35*) using the relation

$$\frac{1}{N\beta}\langle T_\tau O(\tau)O(0)\rangle = \int_0^\infty d\omega\, \mathrm{Re}\, L_{OO}(\omega)\frac{\omega\cosh[\omega(\tau-\beta/2)]}{\pi\sinh[\beta\omega/2]}, \tag{S11}$$

which can be derived from Eqs. S9 and S10. $\mathrm{Re}\, L_{OO}(\omega)$ is guaranteed to be positive definite in Eq. S9. In this work, we measure $\langle T_\tau O(\tau)O(0)\rangle$ and apply MaxEnt for $O \in \{J_x$, $J_{Q,x}$, $J_{K,x}$, $J_{P',x}$, $\lambda_Q J_{Q,x}+J_x$, $\lambda_K J_{K,x}+J_x$, $\lambda_{P'}J_{P',x}+J_x\}$. Here, "$x$" is the x direction and $J_{P',x}$ is defined as $J_{P,x}-\mu J_x$. λ_Q, λ_K and $\lambda_{P'}$ are non-zero real constants.

The kinetic/potential contribution to the DC longitudinal thermal conductivity under the condition of zero electrical current is (*35*)

$$\kappa_{K/P} = \beta^2\left(L_{J_{K/P,x}J_{Q,x}} - \frac{L_{J_{K/P,x}J_x}L_{J_xJ_{Q,x}}}{L_{J_xJ_x}}\right), \tag{S12}$$

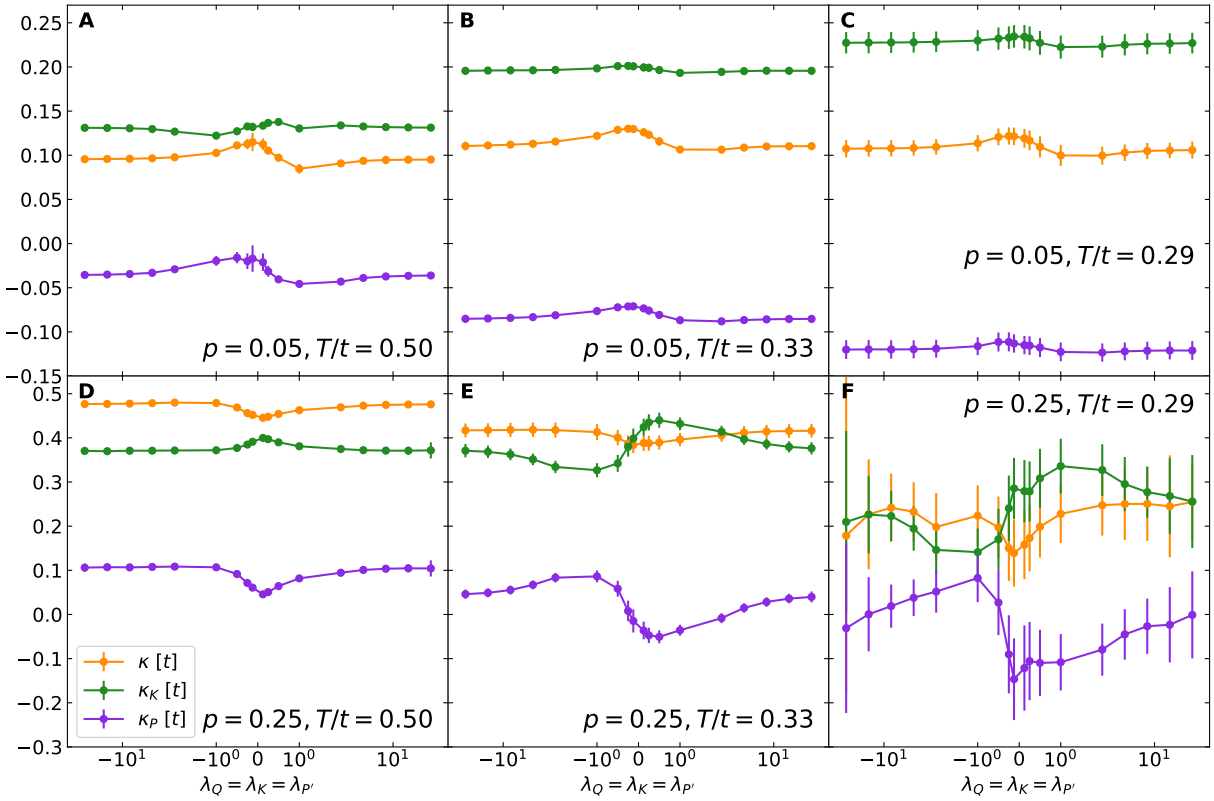

Figure S1: λ_Q, λ_K, and $\lambda_{P'}$-dependence of κ, κ_K and κ_P for a few sets of different doping p and temperature T. Here, λ_Q, λ_K, and $\lambda_{P'}$ are kept the same. For MaxEnt analytic continuation, a flat model function is used for all parameters. Parameters: $U/t = 8$ and $t'/t = -0.25$.

where the DC transport coefficient $L_{O_1O_2}$ is the $\omega = 0$ value of Eq. S7 and is purely real. Here, for κ_P, we transform Eq. S12 to

$$\kappa_P = \beta^2 \left(L_{J_{P',x}J_{Q,x}} - \frac{L_{J_{P',x}J_x} L_{J_xJ_{Q,x}}}{L_{J_xJ_x}} \right). \tag{S13}$$

Even though the expressions are equivalent, using $J_{P',x}$ instead of $J_{P,x}$ in the relevant transport coefficients is a strategy to reduce error propagation. There are multiple ways to combine correlation functions to obtain the same quantity, as seen in Eq. S12 and Eq. S13. Different choices in real computations can result in different magnitudes for the final statistical error after error propagation. For example, subtracting large quantities that yield a small result can lead to large statistical errors relative to the difference. To reduce the statistical error, we obtain κ via

$$\kappa = \beta^2 \left(L_{J_{Q,x}J_{Q,x}} - \frac{L^2_{J_{Q,x}J_x}}{L_{J_xJ_x}} \right), \tag{S14}$$

where $L_{J_{Q,x}J_x}$ is calculated from (*46*)

$$L_{J_{Q,x}J_x} = \left(L_{(\lambda_Q J_{Q,x}+J_x)(\lambda_Q J_{Q,x}+J_x)} - \lambda_Q^2 L_{J_{Q,x}J_{Q,x}} - L_{J_xJ_x} \right) / (2\lambda_Q). \tag{S15}$$

We define and calculate $\kappa_{K,0}$ and $\kappa_{P',0}$ as

$$\kappa_{K,0} = \beta^2 \left(L_{J_{K,x}J_{K,x}} - \frac{L^2_{J_{K,x}J_x}}{L_{J_xJ_x}} \right), \tag{S16}$$

$$\kappa_{P',0} = \beta^2 \left(L_{J_{P',x}J_{P',x}} - \frac{L^2_{J_{P',x}J_x}}{L_{J_xJ_x}} \right), \tag{S17}$$

where $L_{J_{K,x}J_x}$ and $L_{J_{P',x}J_x}$ are calculated from

$$L_{J_{K,x}J_x} = (L_{(\lambda_K J_{K,x}+J_x)(\lambda_K J_{K,x}+J_x)} - \lambda_K^2 L_{J_{K,x}J_{K,x}} - L_{J_xJ_x})/(2\lambda_K), \tag{S18}$$

$$L_{J_{P',x}J_x} = (L_{(\lambda_{P'} J_{P',x}+J_x)(\lambda_{P'} J_{P',x}+J_x)} - \lambda_{P'}^2 L_{J_{P',x}J_{P',x}} - L_{J_xJ_x})/(2\lambda_{P'}). \tag{S19}$$

Then from Eqs. S12, S13, S14, S16, and S17, we have

$$\kappa_K = \kappa_{K,0} + (\kappa - \kappa_{K,0} - \kappa_{P',0})/2, \tag{S20}$$

$$\kappa_P = \kappa_{P',0} + (\kappa - \kappa_{K,0} - \kappa_{P',0})/2, \tag{S21}$$

which are used for the calculation of κ_K and κ_P. If all transport coefficients $L_{O_1O_2}$ are exact, then results for κ, κ_K and κ_P are independent of the choices for λ_Q, λ_K, and $\lambda_{P'}$. However, systematic and statistical errors in $L_{O_1O_2}$ propagate to κ, κ_K and κ_P, so they exhibit some degree of λ_Q, λ_K, and $\lambda_{P'}$ dependence (Fig. S1). Here $\lambda \equiv \lambda_Q = \lambda_K = \lambda_{P'}$. As long as $\lambda \gtrsim 1$, the λ dependence is relatively weak. Therefore, as a reasonable choice, $\lambda_Q = \lambda_K = \lambda_{P'} = 2$ is

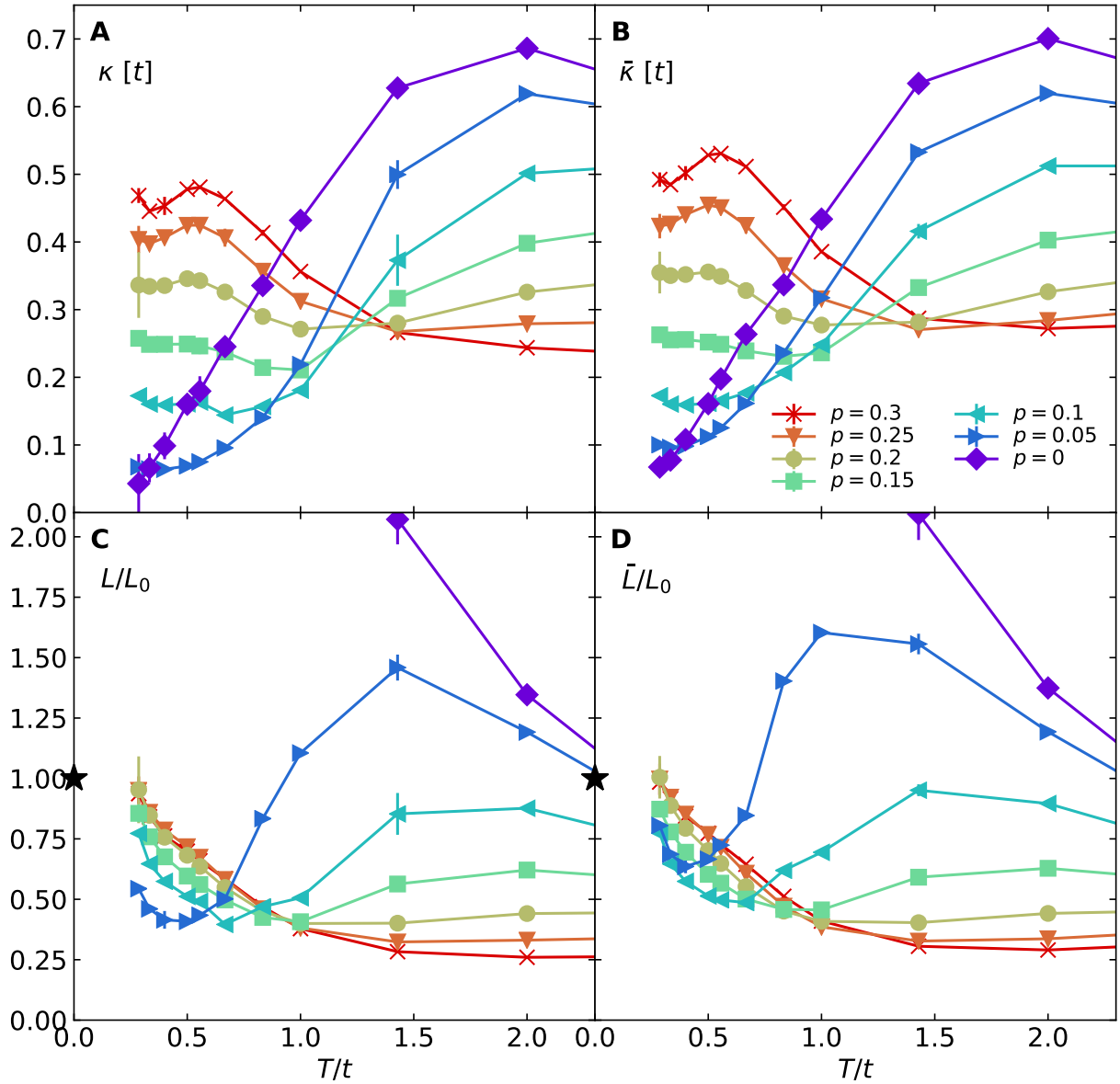

Figure S2: (**A**) DC thermal conductivity κ for zero charge current, the same as Fig. 1(**A**) in the main text. (**B**) DC thermal conductivity $\bar{\kappa}$ for zero electric field. (**C**) Lorenz number $L \equiv \kappa/T\sigma$ normalized by $L_0 \equiv \pi^2/3$, the same as Fig. 2 in the main text. (**D**) Lorenz number $\bar{L} \equiv \bar{\kappa}/T\sigma$, also normalized by L_0. Parameters: $U/t = 8$ and $t'/t = -0.25$.

used in this work, except for $T/t \geq 4$, where $\lambda_Q = \lambda_K = \lambda_{P'} = 0.5$ is used. This is because for high temperatures, the chemical potential μ in $J_{Q,x} = J_{E,x} - \mu J_x$ and $J_{P',x} = J_{P,x} - \mu J_x$ has a large magnitude, and $L_{J_{Q,x}J_{Q,x}}$ and $L_{J_{P',x}J_{P',x}}$ are much larger than $L_{J_xJ_x}$. Therefore, relatively small $\lambda_Q = \lambda_K = \lambda_{P'} = 0.5$ were chosen here to reduce error propagation through Eqs. S15 and S19.

The thermal conductivity κ defined under the condition of zero charge current (Eq. S14) can be compared to the thermal conductivity $\bar{\kappa}$ measured under the condition of zero electric field (*35, 45*), where

$$\bar{\kappa} = \beta^2 L_{J_{Q,x}J_{Q,x}}. \tag{S22}$$

Results for κ and $\bar{\kappa}$ are shown in Figs. S2(**A**) and (**B**), respectively, while Figs. S2(**C**) and (**D**) plot the respective Lorenz numbers $L \equiv \kappa/(T\sigma)$ and $\bar{L} \equiv \bar{\kappa}/(T\sigma)$. Using a representative parameter set $U/t = 8$ and $t'/t = -0.25$ as an example, for the low-temperature regime shown in Fig. S2, κ and $\bar{\kappa}$, as well as L and $\bar{L}$, show similar temperature and doping dependence and have similar magnitudes. Therefore the results and conclusions for the Wiedemann-Franz ratio hold for both quantities.

As discussed in Ref. (*35*), the specific heat c_v may be obtained from the average energy $\langle \hat{H} \rangle$ at different temperatures for fixed densities, directly calculating $\delta(\langle \hat{H} \rangle/N)/\delta T$ by choosing a reasonable finite temperature interval δT, or from the energy fluctuations via

$$c_v = \frac{\beta}{N}\left(\Lambda_{\hat{H}\hat{H}} - \frac{\Lambda^2_{\hat{H}\hat{N}}}{\Lambda_{\hat{N}\hat{N}}}\right). \tag{S23}$$

Here, $\Lambda_{O_1O_2} = \beta(\langle O_1O_2 \rangle - \langle O_1 \rangle \langle O_2 \rangle)$. Similarly, the charge compressibility χ can be calculated using the fluctuation method $\chi = \Lambda_{\hat{N}\hat{N}}/N$. Figure S3 shows the DQMC results for (**A**) the specific heat c_v and (**B**) the charge compressibility χ (*26*). Note that in Fig. S3(**A**) the results for c_v are consistent between the finite difference and fluctuation methods.

The Einstein relations may be used to calculate the thermal diffusivity $D_Q \equiv \kappa/c_v$ and charge diffusivity $D \equiv \sigma/\chi$ (*26, 47*), shown in Figs. S3(**C**) and (**D**). (The fluctuation method is used for calculating both c_v and χ when determining both D_Q and D.) There is a cross-over temperature where the doping dependence of D_Q changes, similar to κ; and in the low temperature regime below T_{xo}, D_Q behaves similarly to D with respect to doping and temperature dependence, as well as changes in the value of Hubbard U (see Figs. S4 and S5).

The potential-kinetic separation of the thermal diffusivity, defined as $D_P \equiv \kappa_P/c_v$ and $D_K \equiv \kappa_K/c_v$, is shown in Figs. S3(**E**) and (**F**), respectively. The inverses D_Q^{-1}, $(\kappa/T)^{-1}$, D^{-1}, and σ^{-1} in Fig. S6 reveal strange metallic $\sim T$ behavior in the doped metallic regime, consistent with earlier results (*26*).

D_Q and D are not strictly independent diffusivities in the heat and charge channels due to non-zero thermoelectric effects in our model. From Refs. (*19, 47*), $D_\pm$ are determined by

$$D_+D_- = DD_Q \tag{S24}$$

$$D_+ + D_- = D + D_Q + D_{\text{corr}}, \tag{S25}$$

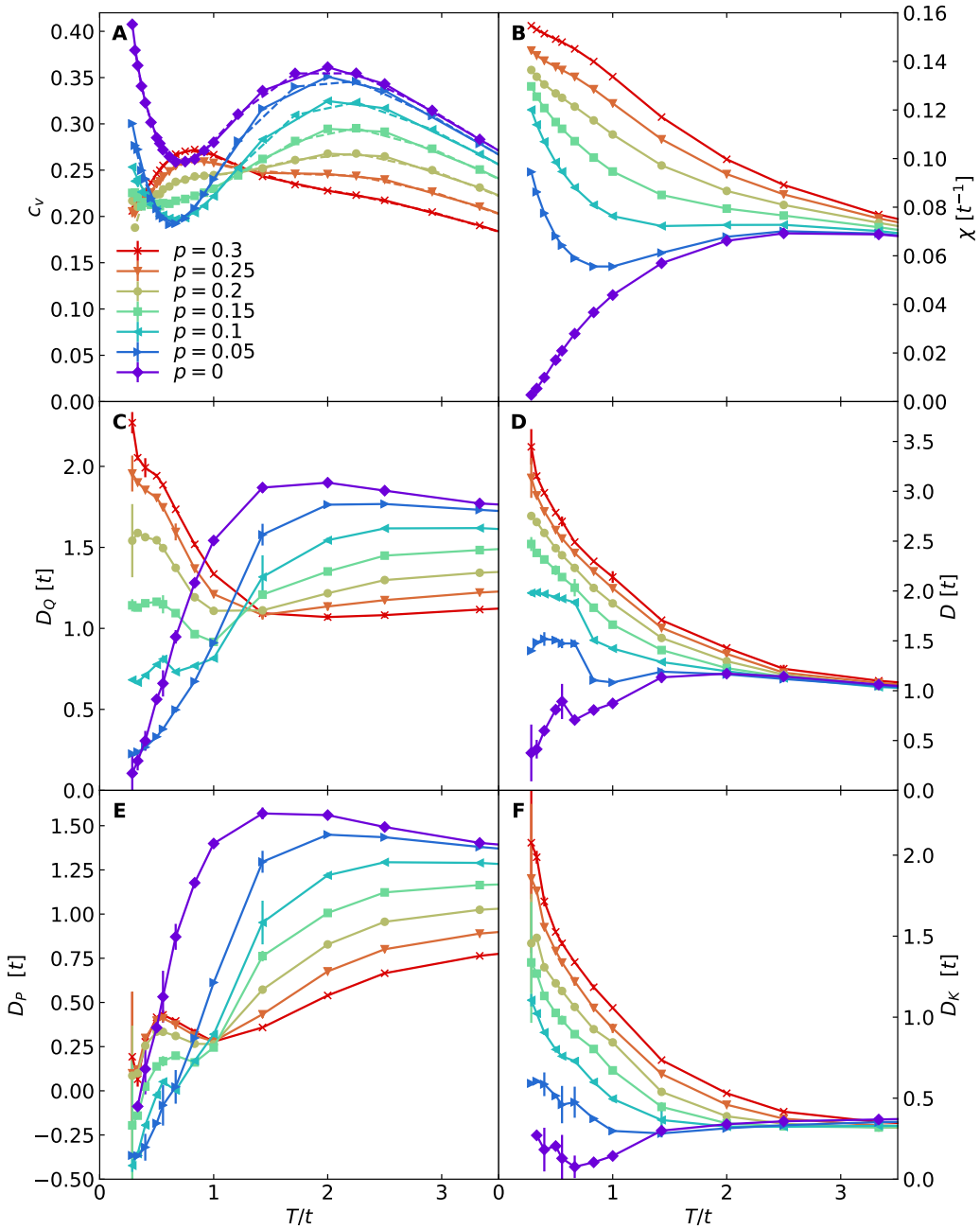

Figure S3: (**A**) Specific heat c_v. Solid lines are results from the fluctuation method and dashed lines are the results from the finite difference method. (**B**) Charge compressibility χ. (**C**) Thermal diffusivity D_Q. (**D**) Charge diffusivity D. (**E**) and (**F**) show the decomposition of thermal diffusivity D_Q into potential D_P and kinetic D_K contributions, respectively. Error bars in (**A**) and (**B**) denote standard error of the mean determined by jackknife resampling. Error propagation is used for c_v obtained from the finite difference method. Parameters: $U/t = 8$ and $t'/t = -0.25$.

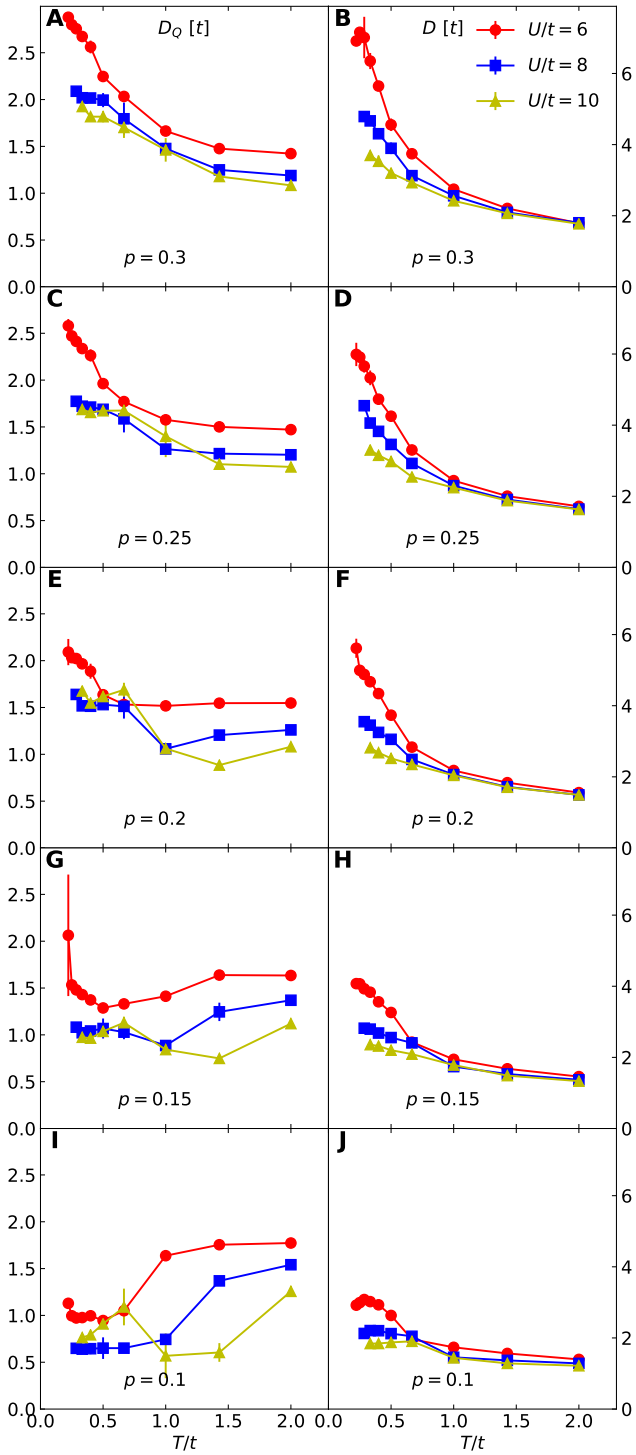

Figure S4: Hubbard U dependence of D_Q and D for $t'/t = 0$. First column is D_Q and the second column is D.

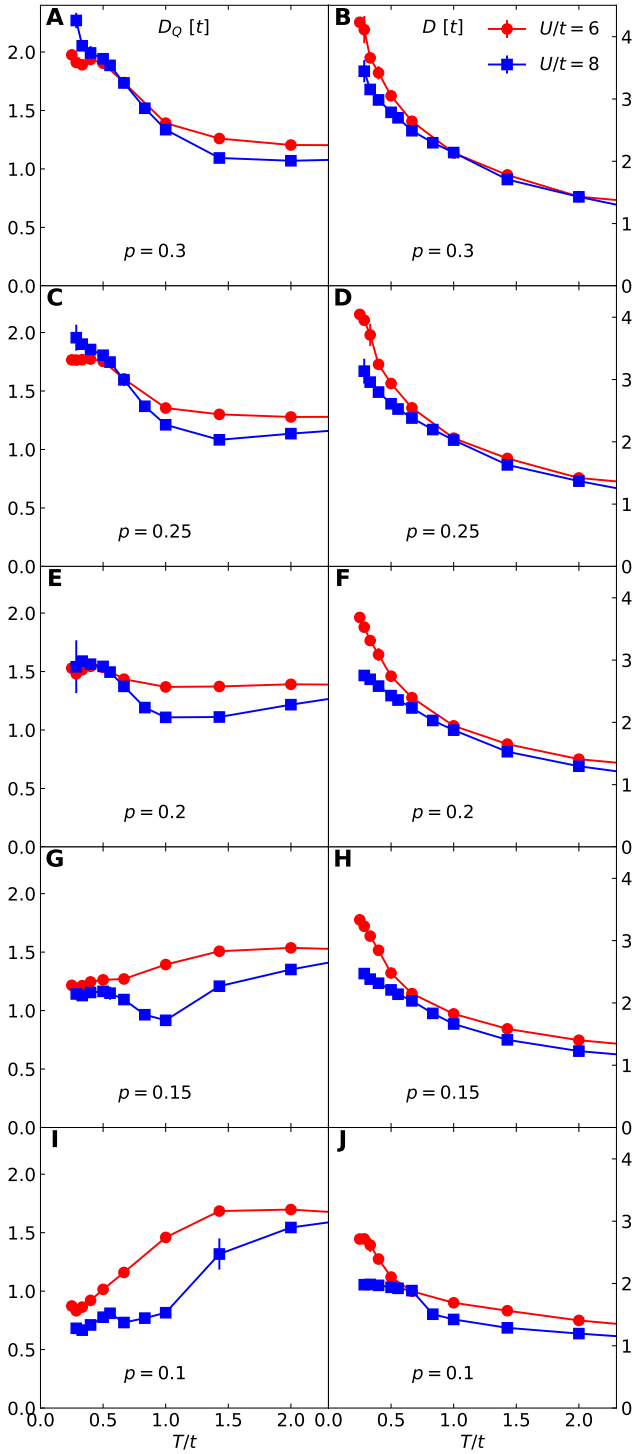

Figure S5: Hubbard U dependence of D_Q and D similar to Fig. S4 but for $t'/t = -0.25$.

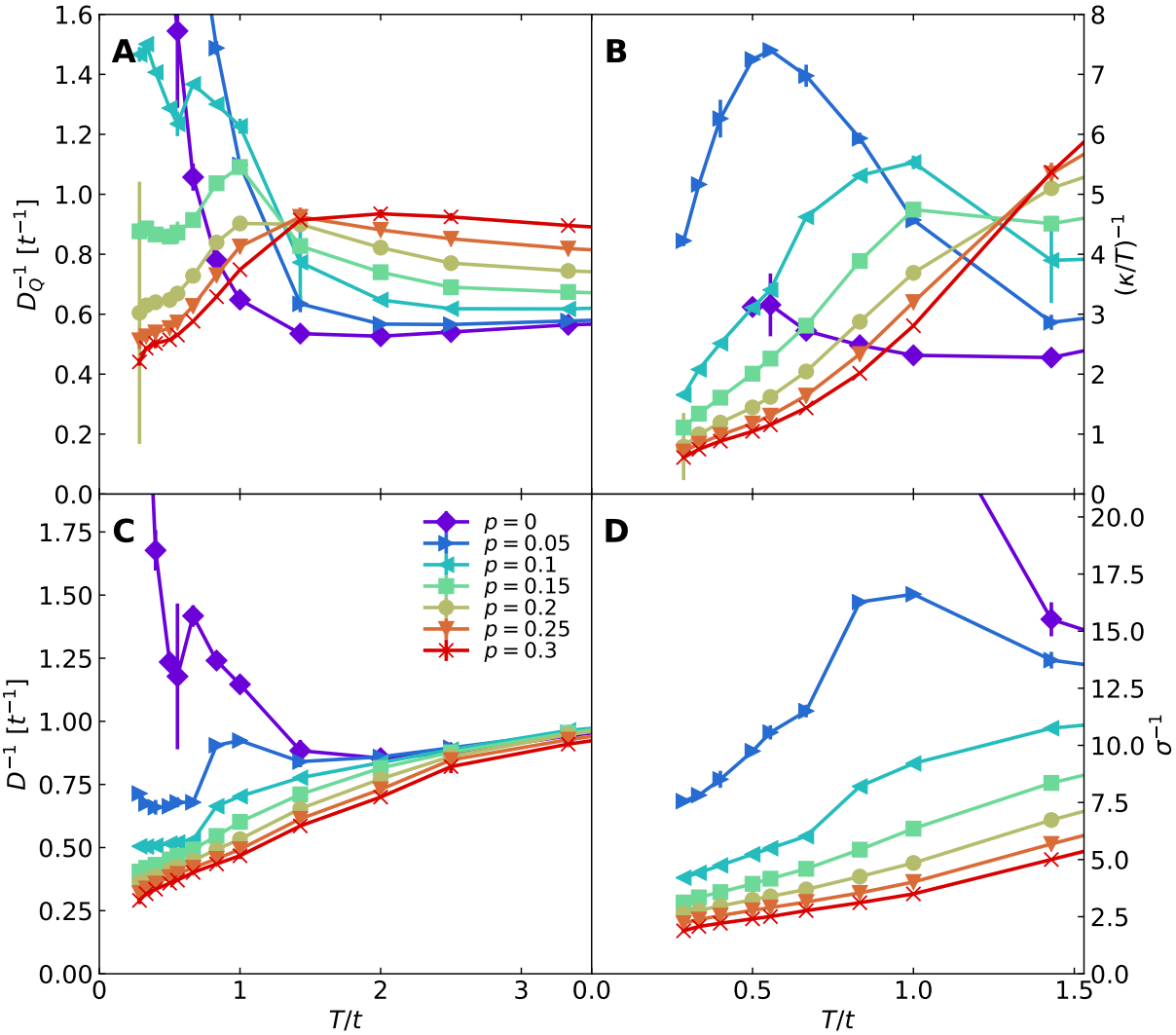

Figure S6: Inverse D_Q, κ/T, D and σ. Parameters: $U/t = 8$ and $t'/t = -0.25$.

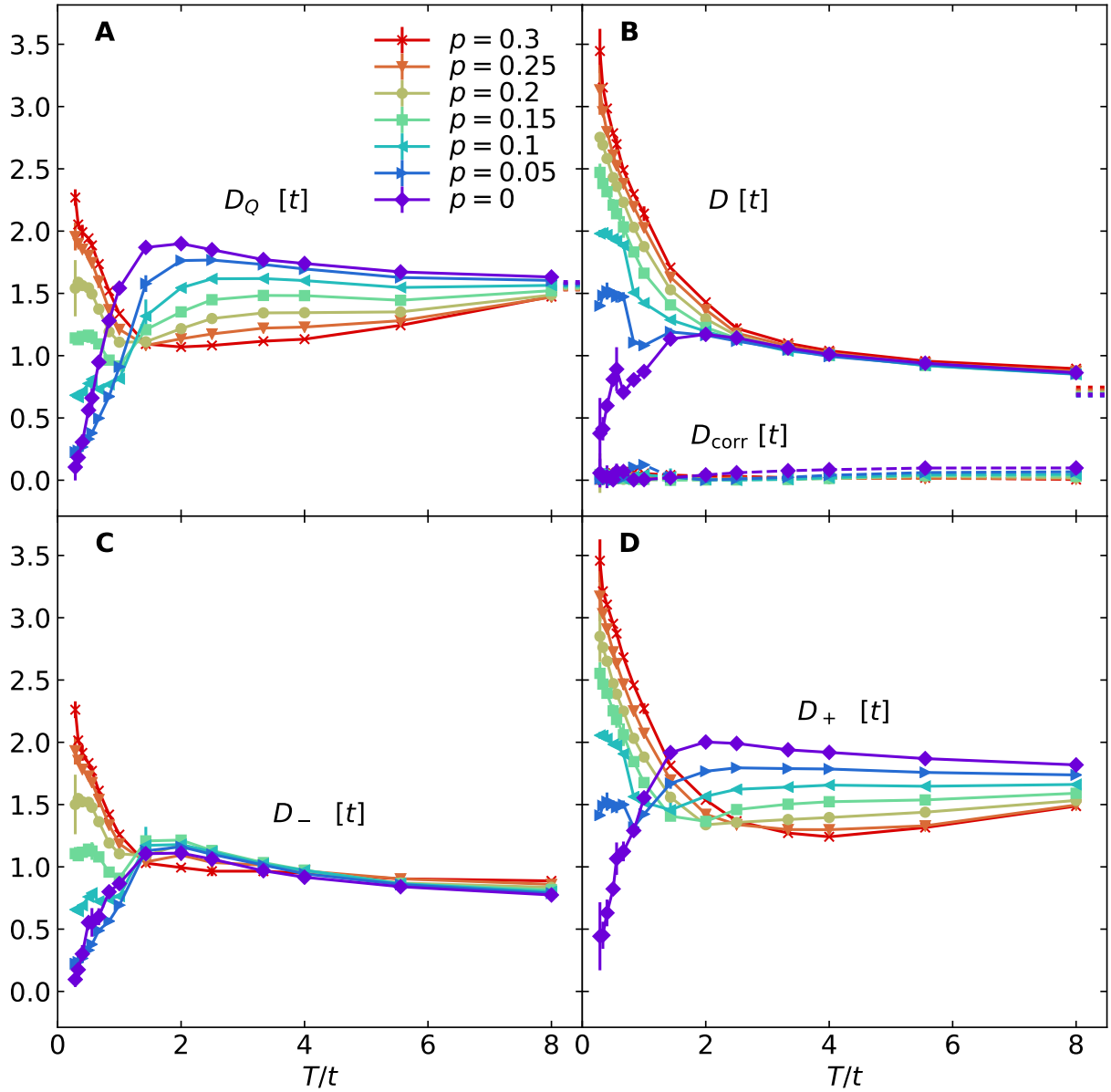

Figure S7: Comparisons between D_Q, D, $D_{\rm corr}$ and $D_\pm$ over a large temperature regime. (**A**) Thermal diffusivity D_Q. (**B**) Charge diffusivity D (solid lines), and correction term $D_{\rm corr}$ (dashed lines). (**C**) D_-. (**D**) D_+. Dotted lines in (**A**) and (**B**) are infinite-temperature limits obtained by the moments expansion method for κ and σ, and analytic calculation for c_v and χ, which will be described later for Fig. S11. Parameters: $U/t = 8$ and $t'/t = -0.25$.

where D_{corr} is the correction term defined in Refs. (*19,47*). Fig. S7 shows that D_{corr} is orders of magnitude smaller than either D_Q or D. Therefore, $D_\pm \approx D$ or D_Q depending on their relative magnitudes. At high temperatures, $D_Q > D$ and $D_+ \approx D_Q$, as shown in Figs. S7(**A**) and (**D**). At low temperatures, $D > D_Q$ and $D_+ \approx D$, shown in Figs. S7(**B**) and (**D**). D_- in Fig. S7(**C**) takes the smaller value between D_Q and D. In the high-temperature limit, D_+ is about twice that of D_-, consistent with Ref. (*47*). Therefore, in our parameter regime, corrections D_{corr} due to thermoelectric effects are negligible compared with D_Q and D, so that D_Q and D are good approximations to the independent diffusivities $D_\pm$.

Model Function Dependence

Model function dependence of the results for the Lorenz number is shown in Fig. S8. Four methods of constructing the model function are analyzed here:

- Method 1: The annealing procedure from high to low temperatures, which is used in the main text.
- Method 2: Annealing from low to high temperatures by starting the procedure using results from method 1 at the lowest temperature as the initial model function.
- Method 3: Using the model functions constructed from the infinite-temperature-limit spectra but with changing chemical potentials for all temperatures.
- Method 4: Using a flat model function for all temperatures.

Fig. S8 shows MaxEnt results obtained using the four methods with qualitatively similar behavior. Therefore, conclusions and the discussion in the main text remain the same regardless of how one constructs the model function in these four distinct ways.

Miscellaneous Supplementary Data

In this subsection a number of checks are presented to support the conclusions given in the main text.

Fig. S9 demonstrates the parameter dependence of the specific heat c_v. The high-temperature peak position of c_v is controlled by the energy scale set by U, similar to that of L in Fig. 3 in the main text.

Fig. S10 plots the kinetic/potential decomposition of L/L_0 for different parameters. For all parameter choices, the kinetic/potential components exhibit behavior similar to Fig. 4 in the main text.

Fig. S11 shows measurements of several quantities up to $T/t = 8$ and compares them to the corresponding infinite-temperature limits. All measurements approach their corresponding infinite-temperature limits as temperature increases. The infinite-temperature limits of the transport properties were calculated using the moments expansion method. The infinite-temperature limits of thermodynamic quantities c_v and χ, given by fluctuations $\Lambda_{O_1O_2}$, were calculated analytically. When $T \to \infty$, $e^{-\beta\hat{H}} = 1$, so $\langle O_1O_2\rangle = \text{Tr}(e^{\beta\mu\hat{N}}O_1O_2)/\text{Tr}(e^{\beta\mu\hat{N}})$ and $\langle O_1\rangle = \text{Tr}(e^{\beta\mu\hat{N}}O_1)/\text{Tr}(e^{\beta\mu\hat{N}})$. The calculation of the right-hand-side traces is straightforward in the occupation basis, when O_1 and O_2 are expressed in fermion operators $c^\dagger_{l,\sigma}$ and $c_{l,\sigma}$.

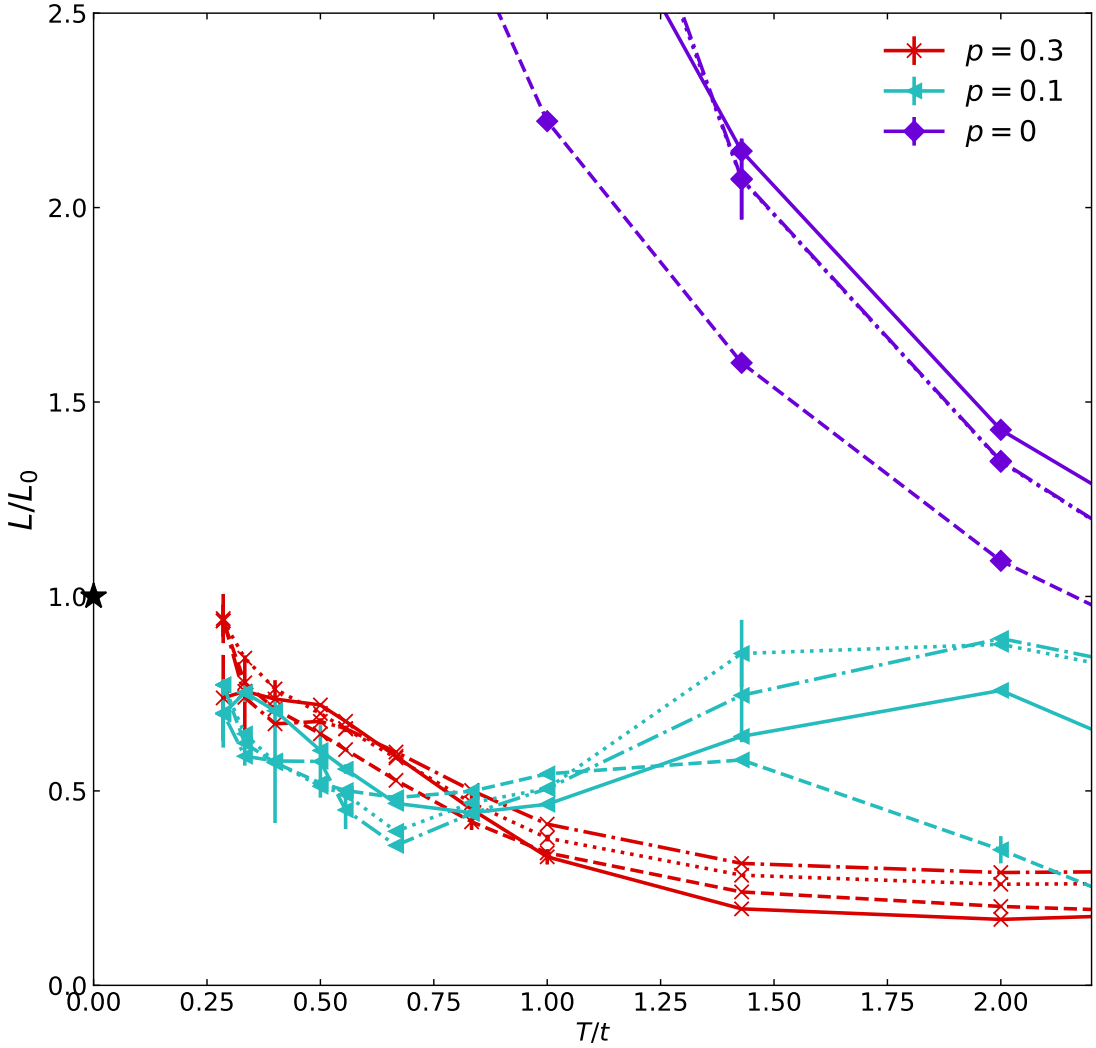

Figure S8: Lorenz number L obtained using method 1 (dotted lines), method 2 (dashed lines), method 3 (dashed dotted lines), and method 4 (solid lines). See the "Model Function Dependence" subsection for definitions of these methods. For $p = 0$ in the displayed range, the dotted line appears hidden as its values are very close to those on the dashed dotted line. Parameters: $U/t = 8$ and $t'/t = -0.25$.

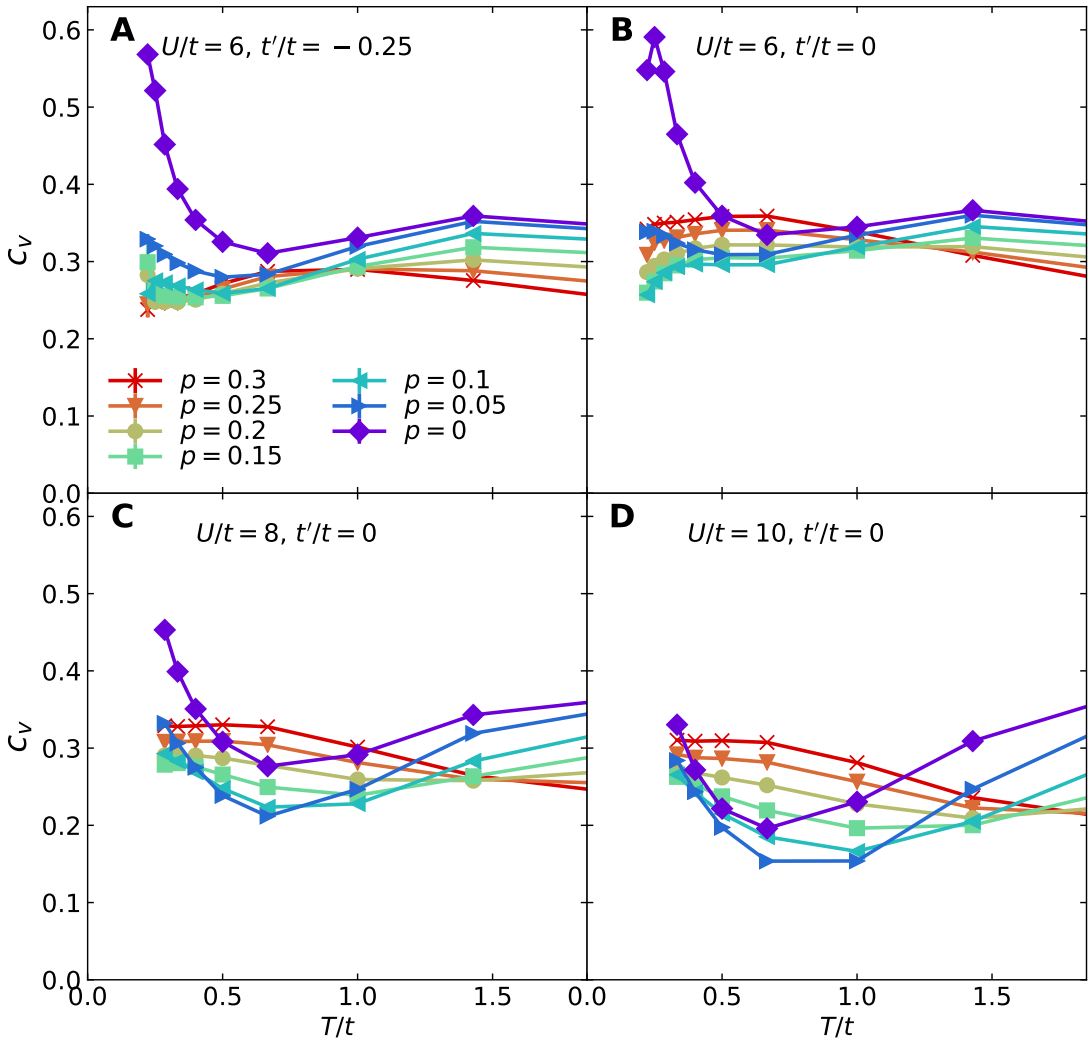

Figure S9: Specific heat c_v obtained via the fluctuation method Eq. S23 for (**A**) $U/t = 6$ and $t'/t = -0.25$; (**B**) $U/t = 6$ and $t'/t = 0$; (**C**) $U/t = 8$ and $t'/t = 0$; (**D**) $U/t = 10$ and $t'/t = 0$.

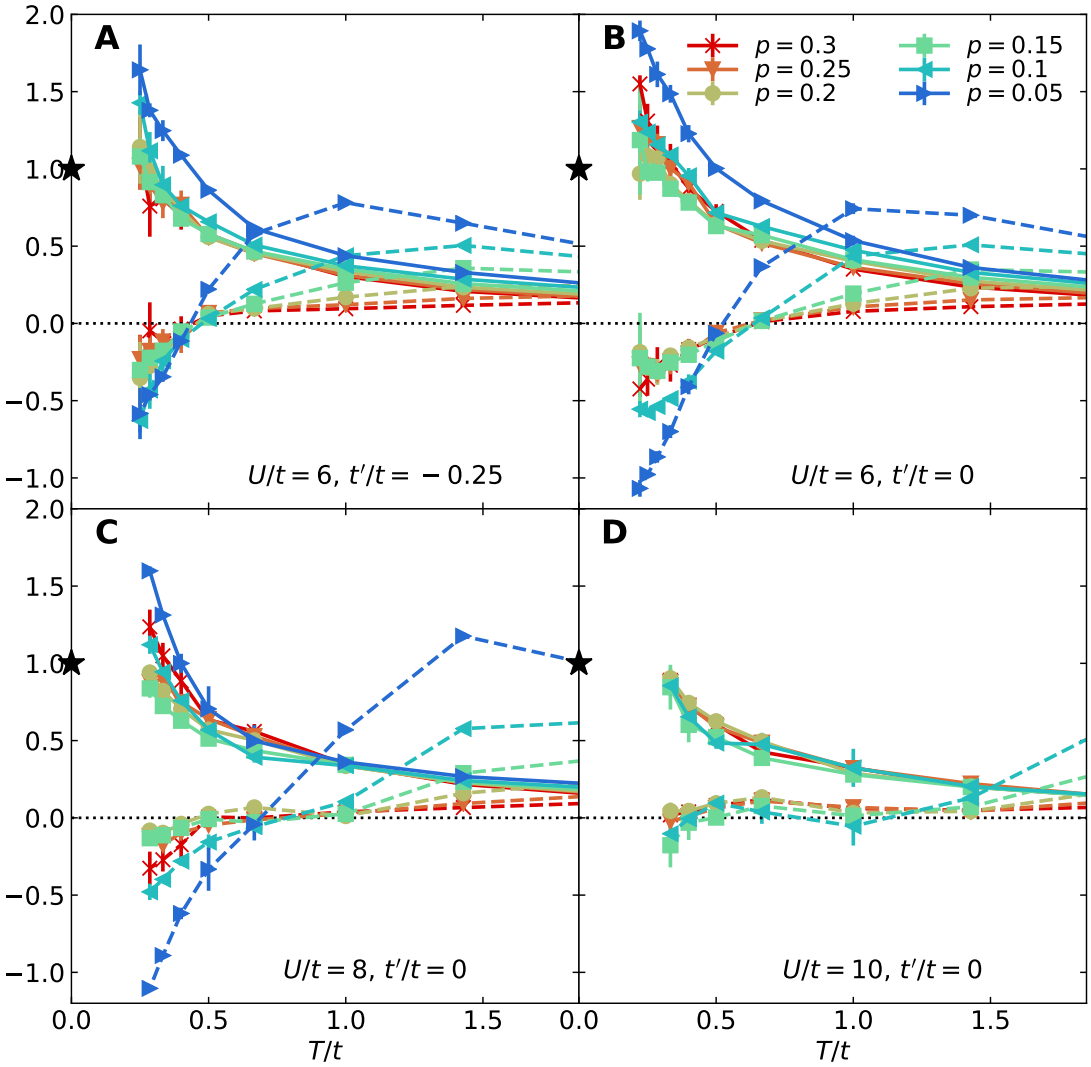

Figure S10: Kinetic/potential decomposition of L/L_0 for (**A**) $U/t = 6$ and $t'/t = -0.25$; (**B**) $U/t = 6$ and $t'/t = 0$; (**C**) $U/t = 8$ and $t'/t = 0$; (**D**) $U/t = 10$ and $t'/t = 0$. Solid lines are L_K/L_0 and dashed lines are L_P/L_0. The black stars mark the value 1. The dotted lines mark the value 0.

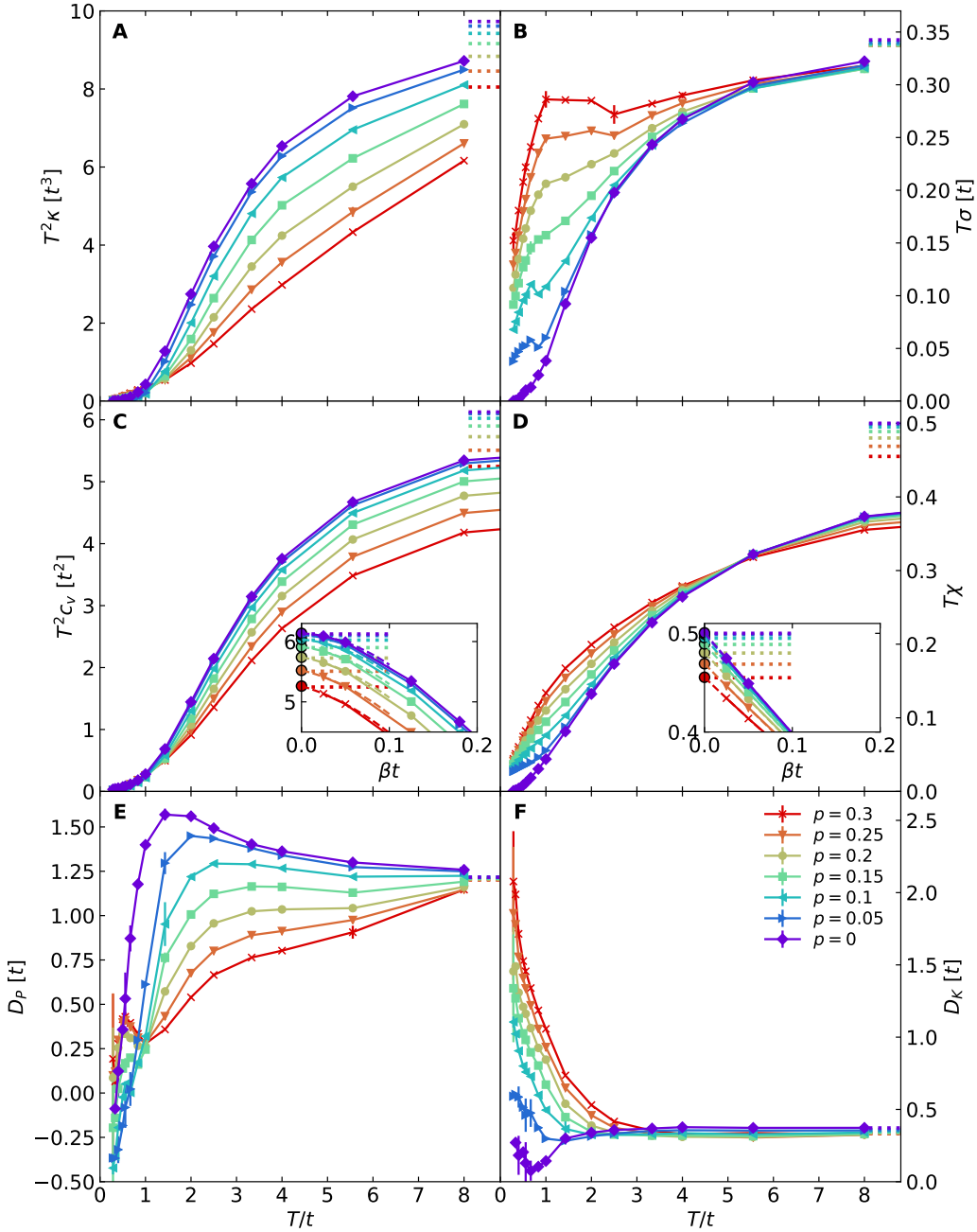

Figure S11: Behavior over a large range of temperatures for (**A**) $T^2\kappa$, (**B**) $T\sigma$ (same data as in Fig. 1(**C**) in the main text), (**C**) T^2c_v (using the fluctuation method), (**D**) $T\chi$, (**E**) D_P, and (**F**) D_K, and a comparison to the infinite-temperature limits for each quantity. Insets for (**C**) and (**D**) are T^2c_v and $T\chi$ versus βt, respectively, and include data for temperatures $T/t \geq 8$. In these insets, dashed lines mark the cubic spline extrapolated function; filled circles mark the extrapolated positions for $\beta t = 0$. The dotted lines in (**A**) to (**F**), including the insets, are infinite-temperature limits. Error bars for T^2c_v and $T\chi$ are from jackknife resampling. Parameters: $U/t = 8$ and $t'/t = -0.25$.

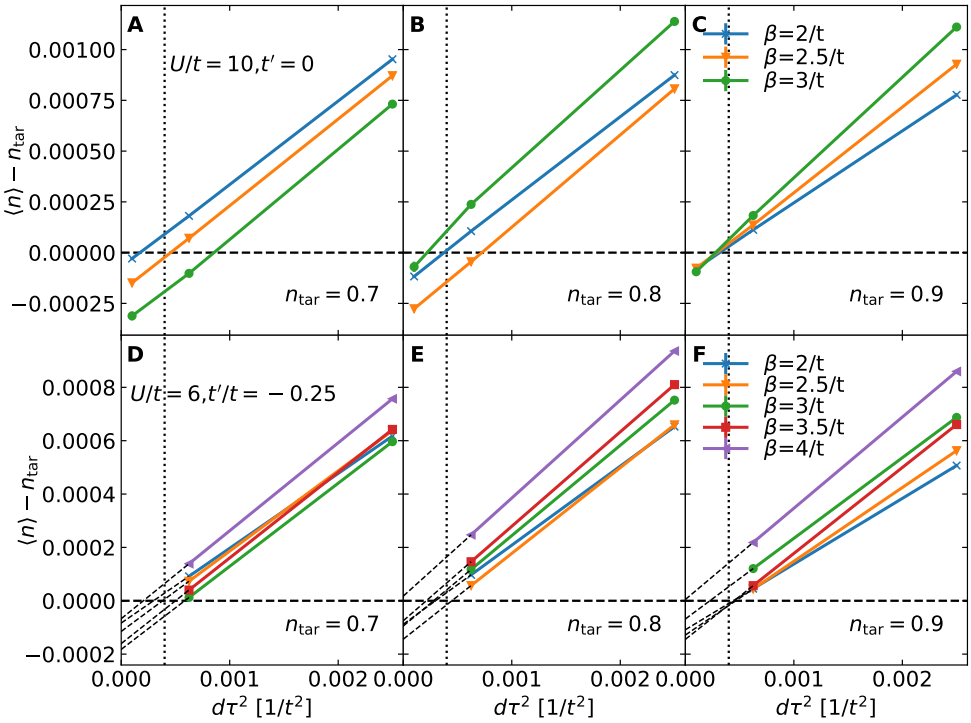

Figure S12: Trotter error analysis for chemical potential tuning. Difference between measured density $\langle n \rangle$ and target density $n_{\rm tar}$ for (**A**)-(**C**) $U/t = 10$, $t'/t = 0$ and (**D**)-(**F**) $U/t = 6$, $t'/t = -0.25$. Vertical dotted lines mark $d\tau = 0.02/t$, which is the discretization interval used for chemical potential tuning. The μ tuned for $n_{\rm tar}$ at $d\tau = 0.02/t$ is used to measure $\langle n \rangle$ for varying values of $d\tau$ on the same curve. Thin dashed lines in (**D**)-(**F**) are straight-line extrapolations as a guide for eye. Thick dashed lines indicate $\langle n \rangle - n_{\rm tar} = 0$. Error bars, which are smaller than the data points, are ± 1 standard error of the mean determined by jackknife resampling.

Trotter Error Analysis

Trotter error enters measurements of thermodynamic and transport properties in two ways. First, it enters in measurements of density $\langle n \rangle$ during chemical potential tuning. After the chemical potential μ is determined for each target density, Trotter error enters in the measurements themselves.

For chemical potential tuning, Fig. S12 shows the difference between the measured density $\langle n \rangle$ and the target density $n_{\rm tar}$ as a function of discretization interval $d\tau$, using μ values obtained from tuning with $d\tau = 0.02/t$. Fig. S12(**A**)-(**C**) shows that the Trotter error scales as $\sim d\tau^2$. Extrapolating $\langle n \rangle - n_{\rm tar}$ to $d\tau^2 = 0$ indicates an estimation of the "true" value of $\langle n \rangle (d\tau = 0) - n_{\rm tar}$, i.e. the systematic error of density due to finite $d\tau = 0.02/t$. For $U/t = 10$, $t'/t = 0$ (the largest U considered in this paper), and $U/t = 6$, $t'/t = -0.25$ (lower temperatures are achievable), the estimated deviation $|\langle n \rangle (d\tau = 0) - n_{\rm tar}|$ is within 10^{-4} as shown in Fig. S12,

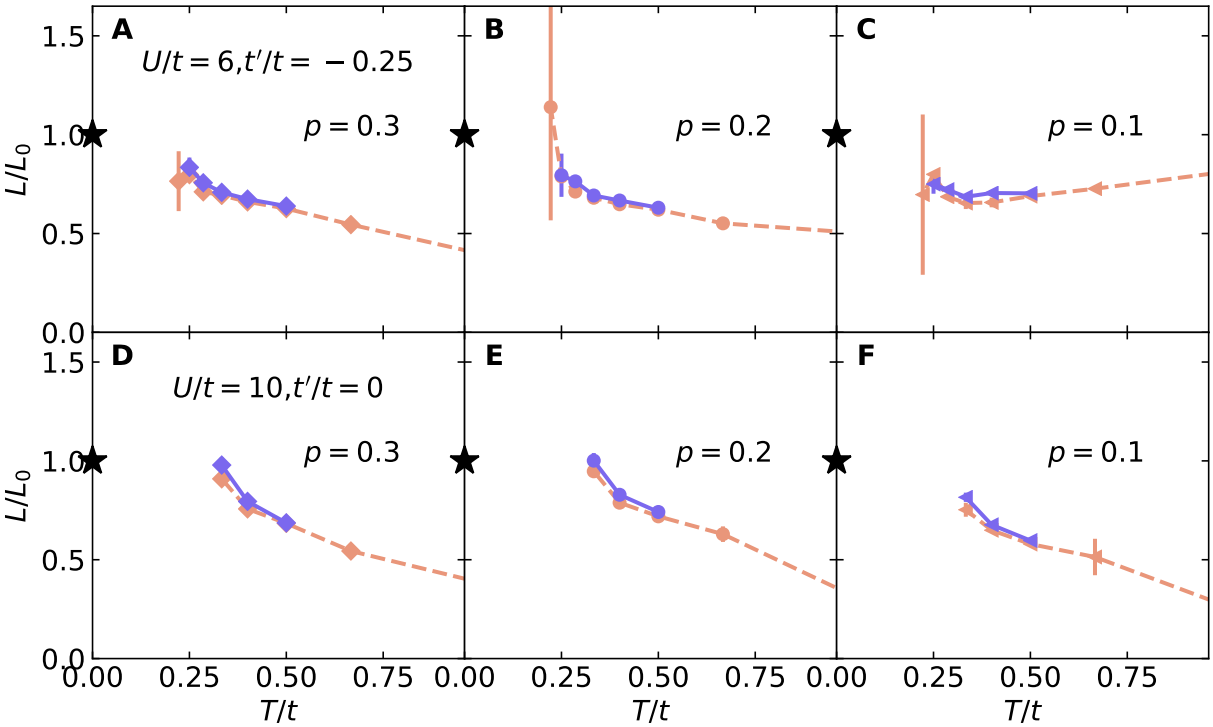

Figure S13: Trotter error analysis of L for (**A**)-(**C**) $U/t = 6$, $t'/t = -0.25$, and (**D**)-(**F**) $U/t = 10$, $t'/t = 0$. Dashed lines are for $d\tau = 0.05/t$ and solid lines are for $d\tau = 0.025/t$.

which represents an upper bound of Trotter error in density for the parameters considered in this paper.

We show the Trotter error for L in Fig. S13, for representative parameters $U/t = 6$, $t'/t = -0.25$ [(**A**)-(**C**)] and $U/t = 10$, $t'/t = 0$ [(**D**)-(**F**)]. Results obtained with $d\tau = 0.05/t$ and $0.025/t$ show minimal difference. For transport measurements, in addition to direct changes in the Trotter error, changing $d\tau$ may affect analytic continuation, as the number of imaginary time points changes for fixed inverse temperature β. Analyzing Fig. S13, we conclude that $d\tau = 0.05/t$ is small enough to prevent Trotter error from affecting our conclusions, and is also a reasonable value for stable MaxEnt analytic continuation.

Finite Size Effects Analysis

In Fig. S14, we compare results of L on 8×8 and 12×12 clusters for $U/t = 6, t'/t = -0.25$, and on 8×8 and 10×10 clusters for $U/t = 8$, $t'/t = -0.25$. The differences between the results are minimal and do not affect our conclusions. A similar finite size analysis for $U/t = 6, t'/t = 0$ is shown in Fig. S15. We observe larger finite size effect for $t'/t = 0$ compared with $t'/t = -0.25$, and for higher doping and lower temperature, because of sharper Drude peaks and more delocalized nature of the system. Lattice size slightly changes the low temperature behaviors of L for $t'/t = 0$, but the overall conclusions are not significantly affected. Smaller U generally should also cause larger finite size effects as the system becomes more delocalized.

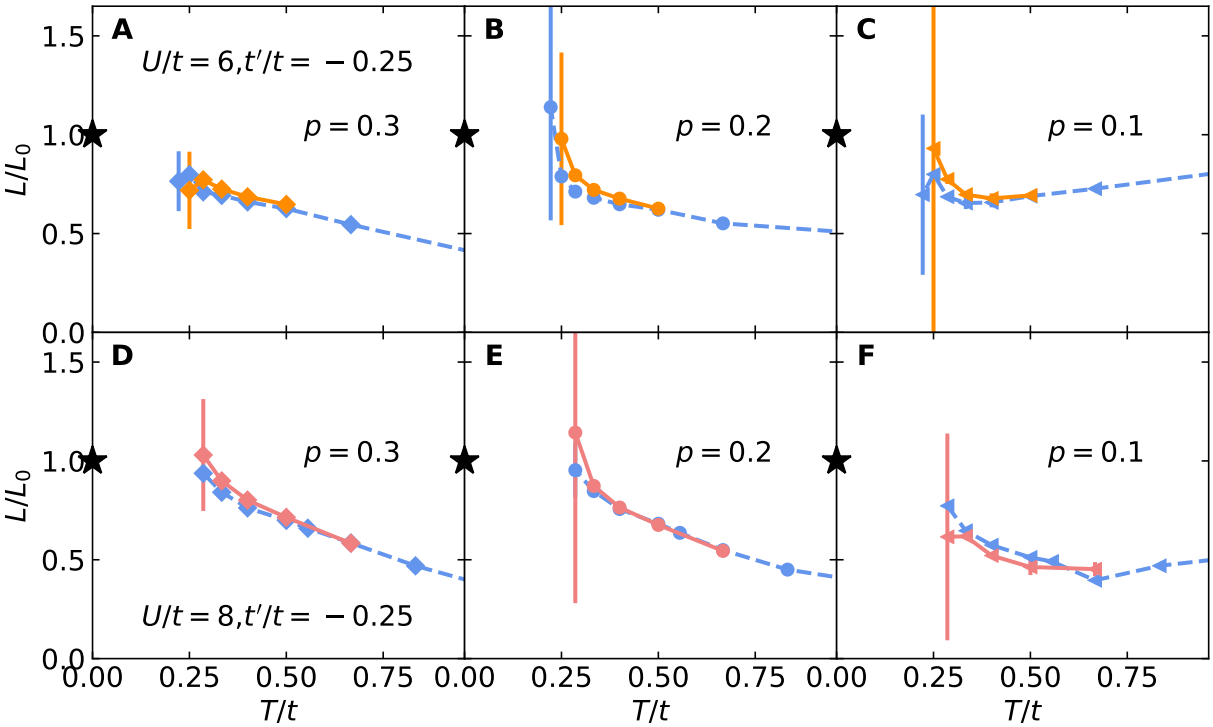

Figure S14: Finite size dependence of L with $t'/t = -0.25$, for (**A**)-(**C**) $U/t = 6$, and (**D**)-(**F**) $U/t = 8$. Dashed lines are obtained on clusters of size 8×8. Solid lines are obtained on clusters of size 12×12 for (**A**)-(**C**) and 10×10 for (**D**)-(**F**).

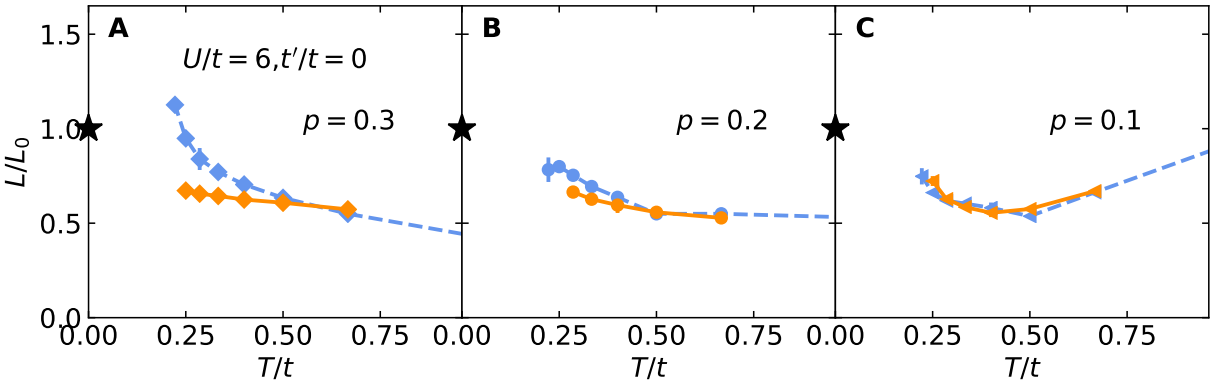

Figure S15: Finite size analysis of L with $t'/t = 0$. Dashed lines are obtained on clusters of size 8×8. Solid lines are obtained on clusters of size 12×12. Simulation parameters: $U/t = 6$, $t'/t = 0$.

Thus, our analysis up to 30% doping, down to $U/t = 6$, including both $t'/t = -0.25$ and $t' = 0$, and down to the lowest accessible temperatures roughly represent an upper bound on the finite size effects, given the parameters considered in this manuscript.

References and Notes

1. O. Gunnarsson, M. Calandra, J. E. Han, *Colloquium*: Saturation of electrical resistivity. *Rev. Mod. Phys.* **75**, 1085–1099 (2003). doi:10.1103/RevModPhys.75.1085

2. N. E. Hussey, K. Takenaka, H. Takagi, Universality of the Mott–Ioffe–Regel limit in metals. *Philos. Mag.* **84**, 2847–2864 (2004). doi:10.1080/14786430410001716944

3. P. W. Phillips, N. E. Hussey, P. Abbamonte, Stranger than metals. *Science* **377**, eabh4273 (2022). doi:10.1126/science.abh4273 Medline

4. J. M. Harris, Y. F. Yan, P. Matl, N. P. Ong, P. W. Anderson, T. Kimura, K. Kitazawa, Violation of Kohler's rule in the normal-state magnetoresistance of $YBa_2Cu_3O_{7-\delta}$ and $La_2Sr_xCuO_4$. *Phys. Rev. Lett.* **75**, 1391–1394 (1995). doi:10.1103/PhysRevLett.75.1391 Medline

5. J. Ayres, M. Berben, M. Čulo, Y.-T. Hsu, E. van Heumen, Y. Huang, J. Zaanen, T. Kondo, T. Takeuchi, J. R. Cooper, C. Putzke, S. Friedemann, A. Carrington, N. E. Hussey, Incoherent transport across the strange-metal regime of overdoped cuprates. *Nature* **595**, 661–666 (2021). doi:10.1038/s41586-021-03622-z Medline

6. T. Kimura, S. Miyasaka, H. Takagi, K. Tamasaku, H. Eisaki, S. Uchida, K. Kitazawa, M. Hiroi, M. Sera, N. Kobayashi, In-plane and out-of-plane magnetoresistance in $La_{2-x}Sr_xCuO_4$ single crystals. *Phys. Rev. B Condens. Matter* **53**, 8733–8742 (1996). doi:10.1103/PhysRevB.53.8733 Medline

7. P. B. Allen, X. Du, L. Mihaly, L. Forro, Thermal conductivity of insulating $Bi_2Sr_2YCu_2O_8$ and superconducting $Bi_2Sr_2CaCu_2O_8$: Failure of the phonon-gas picture. *Phys. Rev. B Condens. Matter* **49**, 9073–9079 (1994). doi:10.1103/PhysRevB.49.9073 Medline

8. R. W. Hill, C. Proust, L. Taillefer, P. Fournier, R. L. Greene, Breakdown of Fermi-liquid theory in a copper-oxide superconductor. *Nature* **414**, 711–715 (2001). doi:10.1038/414711a Medline

9. C. Proust, E. Boaknin, R. W. Hill, L. Taillefer, A. P. Mackenzie, Heat transport in a strongly overdoped cuprate: Fermi liquid and a pure *d*-wave BCS superconductor. *Phys. Rev. Lett.* **89**, 147003 (2002). doi:10.1103/PhysRevLett.89.147003 Medline

10. H. Minami, V. W. Wittorff, E. A. Yelland, J. R. Cooper, C. Changkang, J. W. Hodby, Influence of the pseudogap on the thermal conductivity and the Lorenz number of $YBa_2Cu_3O_x$ above T_c. *Phys. Rev. B Condens. Matter* **68**, 220503 (2003). doi:10.1103/PhysRevB.68.220503

11. S. Nakamae, K. Behnia, N. Mangkorntong, M. Nohara, H. Takagi, S. J. C. Yates, N. E. Hussey, Electronic ground state of heavily overdoped nonsuperconducting $La_{2-x}Sr_xCuO_4$. *Phys. Rev. B Condens. Matter* **68**, 100502 (2003). doi:10.1103/PhysRevB.68.100502

12. C. Proust, K. Behnia, R. Bel, D. Maude, S. I. Vedeneev, Heat transport in $Bi_{2+x}Sr_{2-x}CuO_{6+\delta}$: Departure from the Wiedemann-Franz law in the vicinity of the metal-insulator transition. *Phys. Rev. B Condens. Matter Mater. Phys.* **72**, 214511 (2005). doi:10.1103/PhysRevB.72.214511

13. X. F. Sun, B. Lin, X. Zhao, L. Li, S. Komiya, I. Tsukada, Y. Ando, Deviation from the Wiedemann-Franz law induced by nonmagnetic impurities in overdoped $La_{2-x}Sr_xCuO_4$. *Phys. Rev. B Condens. Matter Mater. Phys.* **80**, 104510 (2009). doi:10.1103/PhysRevB.80.104510

14. G. Grissonnanche, F. Laliberté, S. Dufour-Beauséjour, M. Matusiak, S. Badoux, F. F. Tafti, B. Michon, A. Riopel, O. Cyr-Choinière, J. C. Baglo, B. J. Ramshaw, R. Liang, D. A. Bonn, W. N. Hardy, S. Krämer, D. LeBoeuf, D. Graf, N. Doiron-Leyraud, L. Taillefer, Wiedemann-Franz law in the underdoped cuprate superconductor $YBa_2Cu_3O_y$. *Phys. Rev. B* **93**, 064513 (2016). doi:10.1103/PhysRevB.93.064513

15. J. Zhang, E. M. Levenson-Falk, B. J. Ramshaw, D. A. Bonn, R. Liang, W. N. Hardy, S. A. Hartnoll, A. Kapitulnik, Anomalous thermal diffusivity in underdoped $YBa_2Cu_3O_{6+x}$. *Proc. Natl. Acad. Sci. U.S.A.* **114**, 5378–5383 (2017). doi:10.1073/pnas.1703416114 Medline

16. B. Michon, A. Ataei, P. Bourgeois-Hope, C. Collignon, S. Y. Li, S. Badoux, A. Gourgout, F. Laliberté, J.-S. Zhou, N. Doiron-Leyraud, L. Taillefer, Wiedemann-Franz Law and Abrupt Change in Conductivity across the Pseudogap Critical Point of a Cuprate Superconductor. *Phys. Rev. X* **8**, 041010 (2018). doi:10.1103/PhysRevX.8.041010

17. G. Grissonnanche, A. Legros, S. Badoux, E. Lefrançois, V. Zatko, M. Lizaire, F. Laliberté, A. Gourgout, J.-S. Zhou, S. Pyon, T. Takayama, H. Takagi, S. Ono, N. Doiron-Leyraud, L. Taillefer, Giant thermal Hall conductivity in the pseudogap phase of cuprate superconductors. *Nature* **571**, 376–380 (2019). doi:10.1038/s41586-019-1375-0 Medline

18. J. Zhang, E. D. Kountz, E. M. Levenson-Falk, D. Song, R. L. Greene, A. Kapitulnik, Thermal diffusivity above the Mott-Ioffe-Regel limit. *Phys. Rev. B* **100**, 241114 (2019). doi:10.1103/PhysRevB.100.241114

19. S. A. Hartnoll, Theory of universal incoherent metallic transport. *Nat. Phys.* **11**, 54–61 (2015). doi:10.1038/nphys3174

20. S. A. Hartnoll, A. P. Mackenzie, *Colloquium*: Planckian dissipation in metals. *Rev. Mod. Phys.* **94**, 041002 (2022). doi:10.1103/RevModPhys.94.041002

21. R. Mahajan, M. Barkeshli, S. A. Hartnoll, Non-Fermi liquids and the Wiedemann-Franz law. *Phys. Rev. B Condens. Matter Mater. Phys.* **88**, 125107 (2013). doi:10.1103/PhysRevB.88.125107

22. T. Hartman, S. A. Hartnoll, R. Mahajan, Upper Bound on Diffusivity. *Phys. Rev. Lett.* **119**, 141601 (2017). doi:10.1103/PhysRevLett.119.141601 Medline

23. M. Ulaga, J. Mravlje, P. Prelovšek, J. Kokalj, Thermal conductivity and heat diffusion in the two-dimensional Hubbard model. *Phys. Rev. B* **106**, 245123 (2022). doi:10.1103/PhysRevB.106.245123

24. D. P. Arovas, E. Berg, S. A. Kivelson, S. Raghu, The Hubbard Model. *Annu. Rev. Condens. Matter Phys.* **13**, 239–274 (2022). doi:10.1146/annurev-conmatphys-031620-102024

25. M. Qin, T. Schäfer, S. Andergassen, P. Corboz, E. Gull, The Hubbard Model: A Computational Perspective. *Annu. Rev. Condens. Matter Phys.* **13**, 275–302 (2022). doi:10.1146/annurev-conmatphys-090921-033948

26. E. W. Huang, R. Sheppard, B. Moritz, T. P. Devereaux, Strange metallicity in the doped Hubbard model. *Science* **366**, 987–990 (2019). doi:10.1126/science.aau7063 Medline

27. P. T. Brown, D. Mitra, E. Guardado-Sanchez, R. Nourafkan, A. Reymbaut, C.-D. Hébert, S. Bergeron, A. S. Tremblay, J. Kokalj, D. A. Huse, P. Schauß, W. S. Bakr, Bad metallic transport in a cold atom Fermi-Hubbard system. *Science* **363**, 379–382 (2019). doi:10.1126/science.aat4134 Medline

28. M. A. Nichols, L. W. Cheuk, M. Okan, T. R. Hartke, E. Mendez, T. Senthil, E. Khatami, H. Zhang, M. W. Zwierlein, Spin transport in a Mott insulator of ultracold fermions. *Science* **363**, 383–387 (2019). doi:10.1126/science.aat4387 Medline

29. W. Xu, W. R. McGehee, W. N. Morong, B. DeMarco, Bad-metal relaxation dynamics in a Fermi lattice gas. *Nat. Commun.* **10**, 1588 (2019). doi:10.1038/s41467-019-09526-x Medline

30. R. Blankenbecler, D. J. Scalapino, R. L. Sugar, Monte Carlo calculations of coupled boson-fermion systems. I. *Phys. Rev. D Part. Fields* **24**, 2278–2286 (1981). doi:10.1103/PhysRevD.24.2278

31. S. R. White, D. J. Scalapino, R. L. Sugar, E. Y. Loh, J. E. Gubernatis, R. T. Scalettar, Numerical study of the two-dimensional Hubbard model. *Phys. Rev. B Condens. Matter* **40**, 506–516 (1989). doi:10.1103/PhysRevB.40.506 Medline

32. M. Jarrell, J. E. Gubernatis, Bayesian inference and the analytic continuation of imaginary-time quantum Monte Carlo data. *Phys. Rep.* **269**, 133–195 (1996). doi:10.1016/0370-1573(95)00074-7

33. O. Gunnarsson, M. W. Haverkort, G. Sangiovanni, Analytical continuation of imaginary axis data for optical conductivity. *Phys. Rev. B Condens. Matter Mater. Phys.* **82**, 165125 (2010). doi:10.1103/PhysRevB.82.165125

34. See supplementary materials.

35. W. O. Wang, J. K. Ding, B. Moritz, E. W. Huang, T. P. Devereaux, Magnon heat transport in a two-dimensional Mott insulator. *Phys. Rev. B* **105**, L161103 (2022). doi:10.1103/PhysRevB.105.L161103

36. S. Mukerjee, V. Oganesyan, D. Huse, Statistical theory of transport by strongly interacting lattice fermions. *Phys. Rev. B Condens. Matter Mater. Phys.* **73**, 035113 (2006). doi:10.1103/PhysRevB.73.035113

37. R. E. Prange, L. P. Kadanoff, Transport Theory for Electron-Phonon Interactions in Metals. *Phys. Rev.* **134**, A566–A580 (1964). doi:10.1103/PhysRev.134.A566

38. C. H. Mousatov, S. A. Hartnoll, Phonons, electrons and thermal transport in Planckian high T_c materials. *NPJ Quantum Mater.* **6**, 81 (2021). doi:10.1038/s41535-021-00383-w

39. E. Tulipman, E. Berg, A criterion for strange metallicity in the Lorenz ratio. *npj Quantum Mater.* **8**, 66 (2023). doi:10.1038/s41535-023-00598-z

40. A. Lavasani, D. Bulmash, S. Das Sarma, Wiedemann-Franz law and Fermi liquids. *Phys. Rev. B* **99**, 085104 (2019). doi:10.1103/PhysRevB.99.085104

41. W. O. Wang, Source code for "The Wiedemann-Franz law in doped Mott insulators without quasiparticles," Zenodo (2023). https://doi.org/10.5281/zenodo.7976147.

42. W. O. Wang, Data for "The Wiedemann-Franz law in doped Mott insulators without quasiparticles," Zenodo (2023). https://doi.org/10.5281/zenodo.7976153.

43. D. Bergeron, A.-M. S. Tremblay, Algorithms for optimized maximum entropy and diagnostic tools for analytic continuation. *Phys. Rev. E* **94**, 023303 (2016). doi:10.1103/PhysRevE.94.023303 Medline

44. B. Efron, R. J. Tibshirani, *An Introduction to the Bootstrap* (Chapman & Hall/CRC, 1993).

45. B. S. Shastry, Electrothermal transport coefficients at finite frequencies. *Rep. Prog. Phys.* **72**, 016501 (2008). doi:10.1088/0034-4885/72/1/016501

46. A. Reymbaut, A.-M. Gagnon, D. Bergeron, A.-M. S. Tremblay, Maximum entropy analytic continuation for frequency-dependent transport coefficients with nonpositive spectral weight. *Phys. Rev. B* **95**, 121104 (2017). doi:10.1103/PhysRevB.95.121104

47. C. H. Mousatov, I. Esterlis, S. A. Hartnoll, Bad Metallic Transport in a Modified Hubbard Model. *Phys. Rev. Lett.* **122**, 186601 (2019). doi:10.1103/PhysRevLett.122.186601 Medline